Pore-scale influence of methane hydrate on permeability of porous media

Lingli Pan[1], Liang Lei[1*], Yongkoo Seol[1]

[1]National Energy Technology Laboratory, U.S. Department of Energy, Morgantown, WV, U.S.

[*]Corresponding author: Liang Lei (leiliang@westlake.edu.cn)

Key Points

- Actual hydrate pore habits and distribution are used to numerically simulate single phase flow through methane hydrate-bearing sediments.
- Inter-pore hydrate distribution has a higher impact on permeability than intra-pore habits or hydrate formation method.
- Small hydrate saturation reduces permeability significantly and uneven hydrate distribution results in drastic permeability anisotropy.

Abstract

Influence of methane hydrate on permeability of hosting sediments is critical to understand natural hydrate formation and gas production. A few conceptual models proposed to explain the influence of hydrate could not recapitulate the actual hydrate pore habits and distribution with the overly-simplified geometric assumptions used in those models. This study simulates single phase flow through hydrate-bearing sediments with a numerical approach to explore influences of hydrate on fluid flow, based on real 3D pore structures of methane hydrate-bearing sediments obtained via micro-CT scans. Pore-scale analysis and observations show (1) hydrate particles, at low hydrate saturation, protrude into the flow channels and efficiently inhibit the flow; (2) at

high saturation or in small pores, hydrate particles block some pores and pores without hydrate determine permeability. Influence of intra-pore habit on permeability is not obvious; by contrast, inter-pore distribution of hydrate has a higher impact and can cause drastic permeability anisotropy.

Key words: gas hydrate-bearing sediments, permeability, micro-CT, pore structure, pore habit

Plain Language Summary

While the potential to impact the energy market due to its massive organic carbon reserve in natural gas hydrate is widely accepted, permeability, the most critical parameter to describe how fast fluids can flow through methane hydrate bearing sediments is yet to be clearly understood with respect to its role on formation mechanisms of natural gas hydrate reservoirs and gas production potential. Currently, idealized geometric assumptions are often used in conceptual permeability models to describe hydrate morphology in the pore space, however, such models cannot explain various experimental results because actual hydrate morphology does not meet their assumptions. To consider realistic hydrate morphology, we simulate single phase flow through pore structures extracted from synthesized methane hydrate-bearing specimens using micro CT. High resolution image analysis and numerical modeling reveal that hydrate particles at low saturation protruding into the pore structure efficiently reduce the flow velocity, and at higher saturation, hydrate particles block most paths and the flow is restricted to less paths. This study highlights that rather than intra-pore habit of hydrate resulted from hydrate formation method, permeability of hydrate-bearing sediments is more impacted by inter-pore hydrate distribution and uneven hydrate distribution can result in permeability anisotropy.

1 Introduction

Gas hydrate is a crystalline compound made of water and guest molecules (Makogon, 1997; Sloan & Koh, 2007). Natural gas hydrate, due to its massive reserve in nature, is regarded as a potential energy resource and environmental hazard if released to the atmosphere (Boswell, 2009; Boswell & Collett, 2011; Milkov, 2004). Mass transfer within hydrate-bearing sediments is critical for understanding formation and dissociation of hydrate in natural reservoirs (Li et al., 2016; Wang et al., 2018; You et al., 2019), and fluid flow is a key mechanism controlling the mass transfer. Various models have been developed for fluid flow in hydrate-bearing sediments as a function of hydrate saturation: some assume idealized hydrate distributions such as grain-coating or pore-filling (Kleinberg et al., 2003; Singh et al., 2019), and some involve empirical relations (Chen et al., 2018; Dai & Seol, 2014; Masuda, 1997). Yet the scattered laboratory results from the literature cannot be predicted by these models (Berge et al., 1999; Delli & Grozic, 2014; Johnson et al., 2011; Kleinberg et al., 2005; Kneafsey et al., 2011; Konno et al., 2015; Kumar et al., 2010; Lee, 2008; Liang et al., 2011; Liu et al., 2017; Mahabadi et al., 2019; Minagawa et al., 2012; Priest et al., 2015; Ren et al., 2020; Sakamoto et al., 2003; Santamarina et al., 2015). One major reason that caused this gap between proposed models and laboratory results is that the assumptions on hydrate pore habits and distribution are overly simplified and do not capture complexity of real mass flow phenomena occurring within pore structure in the presence of methane hydrate.

Owing to the recent developments of micro-CT technique, pore-scale 3D structure of hydrate-bearing sediments can be obtained, first on specimen formed with surrogate guest molecules (Chaouachi et al., 2015) and recently on methane hydrate-bearing sediments (Lei et al., 2019b) with heavy salt doping technique (Lei et al., 2018). The 3D pore structure can be isolated and

used to simulate fluid flow through hydrate-bearing sediments. However, these results are mostly on xenon or krypton hydrates formed under excess-gas conditions (Chen et al., 2018). Result on methane hydrate-bearing sediments, especially prepared under excess-water condition (often considered as that in natural reservoirs), is rare.

This work simulates single phase fluid flow through pore structures obtained from laboratory synthesized methane hydrate-bearing sediments with micro-CT technique. The hydrate formation conditions include excess-gas, excess-water and a transition from excess-gas to excess-water to account for the effect of pore habit. Results are explained based on pore-scale observations.

2 Methods

Figure 1 presents the procedure to obtain velocity field from raw CT images.

Image data collection and interpretation. Raw CT images are from experiments conducted at National Energy Technology Laboratory (Lei & Seol, 2019, 2020; Lei et al., 2019b), and hydrate-bearing specimens were prepared with three different methods (Table 1). These 21 tests are selected to cover different formation methods and various hydrate saturations. Following are the description on hydrate formation methods and issues related to image interpretation. (1) Excess-gas: sand and water was mixed first and then pressure and temperature were adjusted to form hydrate while methane was supplied with constant pressure. The resultant specimen contains sand particles, methane hydrate and free methane. The connected pore space occupied by free methane is segmented and used as pore structure for fluid flow in simulations. We cannot exclude the possibility of free water left inside the specimen, but even if free water exists, it should be covered by methane hydrate as any direct contact between gas and water would result in hydrate formation when the temperature-pressure is within hydrate stability field. Therefore,

the potential existence of free water does not affect the simulation result. Hydrate saturation in this case may include such potential free water. (2) Excess-water from excess-gas: brine (5 wt% of potassium iodide solution) was injected through the hydrate-bearing specimens to replace free methane. The simulation was based on the connected water path. Note there are always free methane enclosed by methane hydrate that does not fully transform into hydrate (Lei et al., 2019c). We consider that the space occupied by free gas does not contribute to fluid flow and the hydrate saturation includes free gas. (3) Excess-water: high pressure methane and water coexist at the beginning and then water was supplied under constant pressure, so that methane was limited during hydrate formation. The connected water path is used for simulation and hydrate saturation includes the enclosed free gas.

Hydrate formation does not alter the sand skeleton, i.e., pore structure, under constant effective stress condition. Therefore, the effect of hydrate can be evaluated by considering two cases: (1) Without-hydrate, where the pore structure includes space occupied by all pore constituents (water and gas) to obtain intrinsic permeability k_0; (2) With-hydrate, where the pore structures are described in the previous paragraph to calculate effective permeability k_e.

Model construction and boundary conditions. A cube consisted of ~345^3 voxels with a resolution of ~4.6 μm is the solving domain, in which pressure gradients are applied across two corresponding faces in the principal direction while treating all other faces as isolated peripheral boundaries. The voxelized structures are obtained from the segmentation, with ilastik (Berg et al., 2019), of micro-CT images of laboratory synthesized methane hydrate-bearing specimens. Finite-Difference Method Stokes Solver (FDMSS) (Gerke et al., 2018) is used to solve Stokes equation directly on voxelized 3D pore structures and thus calculate a 3D velocity field and permeability. Paraview (Ayachit, 2015) and 3D Slicer (Kikinis et al., 2014) are used for results

visualization. Simulations are run in three different principal directions. Note that simulations on voxelized pore structures is accompanied with errors due to voxelization (model calibration and error analysis are covered in the Supporting Material).

3 Results and Discussion

This section compares simulation results with previously proposed models based on simplified geometry assumptions and attempts to explain the results according to pore-scale observations.

3.1 Permeability versus hydrate saturation

This work focuses on the effect of methane hydrate on permeability, therefore the ratio between effective permeability and intrinsic permeability k_e/k_0, referred as normalized permeability k, is plotted against hydrate saturation in Figure 2, together with predictions from models in Kleinberg et al. (2003). It seems that most of the simulation results match well the prediction of pore-filling assumption (KP and CP in Figure 2), and the influence of hydrate formation method is not obvious, although the pore habit under excess-gas condition is known to be different from that under excess-water condition (Lei et al., 2019b). Meanwhile, some results at some hydrate saturations (examples in green frames in Figure 2) show clear anisotropy, i.e., the permeability along X, Y and Z direction differs. The following sections explore pore-scale explanations for these observations.

3.2 Observed methane hydrate morphology versus idealized assumptions

Idealized pore habit is used in model derivation for Kleinberg et al. (2003): pore-filling assumes hydrate floats yet unrealistically anchors in the middle of tube or pore center; similarly, grain-

coating considers hydrate coating particle/tube surfaces with uniform thickness. These models have been widely used, yet observed hydrate pore habit does not agree with the idealized assumptions. In fact, hydrate can never float in the pore center, since the density of methane hydrate is less than water. Hydrate is always in contact with sediment particles (note that some of the hydrate particles in Figures 1, and 3-5 appear floating only due to the angle of cutting plane in 3D matrix). The affinity of pore constituents to quartz sand surface follows the order of water/brine, methane hydrate and free methane from highest to least, which is supported by the observation that the contact angle of methane hydrate to quartz surface is on average 120° and 72° in excess-water and excess-gas environments (Lei et al., 2019b). Therefore, the pore habit of methane hydrate leans toward cementing and grain-coating in excess-gas environments, but pore-filling in excess-water environments. We highlight the difference between idealized assumptions and actual hydrate behavior but the terms grain-coating and pore-filling are still used here to follow the tradition. Brine injection to change the condition from excess-gas to excess-water would transfer pore habit towards pore-filling, which suggests that hydrate distribution and pore habit are influenced by hydrate formation history.

3.3 Effect of hydrate on velocity field

Figure 3 shows hydrate's influence on velocity fields at two different hydrate saturations. At low saturation, 8.0% in Figure 3a (one major path cut open for visualization), hydrate particles can behave as thrombus attached on sand particles, protrude into the pore space and efficiently reduce the flow velocity. We simplify the actual hydrate distribution into a relatively realistic model as shown in Figure 3b (hydrate particles considered as individual thrombus in a tube, details in Supplemental Material). With multiple hydrate particles protruding into the pore

structure, a small hydrate saturation (8.0% here) can reduce the permeability by 50.8% (green cross mark in Figure 2). As shown, the flow path is narrowed much more efficiently than that with the idealized uniform grain-coating. The result of this model is closer to the prediction with pore-filling, although the geometry is not even close to the idealized pore-filling form. We highlight that this thrombus-like hydrate distribution can explain some experimental results that are previously thought to be caused by pore-filling pore habit.

At high saturation, 71.5% in Figure 3c, hydrate particles block some paths completely and the flow is restricted to limited paths. The hydrate pore habit is not critical at this level of hydrate saturation because hydrate often either completely fills the pore or leaves it open (Figure 3c.2), known as patchy hydrate distribution (Dai et al., 2012). The dominant factor is the connectivity of the pores in pore structure after hydrate accumulation. Flow path clogging starts at a minimum hydrate saturation of ~68% (Table 1 and Figure 2). Note that complete clogging is statistically less likely to occur as model size increases.

3.4 Permeability anisotropy

Figure 4 shows the velocity field of Test 17 along X, Y, and Z directions. The original pore structure before hydrate formation does not show obvious permeability anisotropy. But when hydrate forms and preferentially accumulates on the right side (positive X direction), the flow along X direction is greatly reduced, while the flow paths along Y and Z directions locally concentrates on the left side. Permeability anisotropy caused by hydrate accumulation is confirmed in our simulations. Uneven hydrate distribution occurs commonly in hydrate formation, due to initial uneven water/gas distribution (Ren et al., 2020), or cryogenic suction associated with temperature gradient (Lei et al., 2019a), or Ostwald ripening (Chen & Espinoza,

2018). If permeability is measured in hydrate-bearing specimens with uneven hydrate distribution, results along certain directions could be close to grain-coating or pore-filling predictions (permeability values spread in Figure 2); but this does not provide evidence to indicate the hydrate pore habit. This highlights the critical role of inter-pore hydrate distribution in affecting permeability.

3.5 Permeability in layered systems

Figure 5 shows hydrate distribution in two layers of sand in Tests 5 and 12 (Ottawa sand with ~ 250μm diameter at bottom and F110 with ~ 120μm at top) and its influence on fluid flow. Hydrate forms under excess-gas condition initially, and the hydrate saturation in F110 is higher due to the higher water content available for hydrate growth (Figure 5b.1). Brine injection, to replace free methane, alters the environment from excess-gas to excess-water and triggers relatively more hydrate formation in F110 with a larger amount of trapped methane (Figure 5c.1). The preferential hydrate formation in F110 layer promotes the permeability anisotropy (Figure 2). This pattern could occur in actual reservoirs as natural gas hydrate could occur in geologic formations with non-uniform compositions and layering as seen in India and Gulf of Mexico (Fang et al., 2020; Nanda et al., 2019; Phillips et al., 2020), where permeability anisotropy would have obvious impacts (Lei et al., 2019c).

Hydrate particle size is similar in Ottawa sand and F110 (Lei et al., 2019b). This hydrate particle size is smaller than the pore size in Ottawa sand, therefore, it is possible for hydrate habit, whether grain-coating or pore-filling, to have an influence on permeability; although the influence of pore habit is not obvious in this study. By contrast, hydrate particle size is comparable to pore size in F110, therefore, hydrate particles often completely fill pores, altering

flow paths rather than narrowing original flow paths. Therefore, the connectivity of the unfilled pores, rather than hydrate habits within the pore, is more important in determining fluid permeability in such finer sediment. This is particularly important because sediments in a large portion of hydrate reservoirs targeted for gas production are within the range of fine-sand to silt (Nanda et al., 2019; Phillips et al., 2020), and the pore size could be smaller than that in F110.

3.6 Pore habit and permeability

Figure 2 shows that for relatively homogenously distributed hydrate, permeabilities of hydrate-bearing sediments prepared under excess-gas condition or excess-water condition do not show distinctive correlation to the hydrate formation methods. Previously in Section 3.2, it was shown that the actual pore habit is not ideal as proposed by geometric conceptual model and such over-simplified pore habit models would be insufficient to explain permeability variations. In addition, initial water menisci in excess-gas systems promotes hydrate formation at pore throats (Mahabadi et al., 2019), and hydrate in excess-water systems preferentially occupies large pores (Lei et al., 2019b); both of which enhances the role of hydrate in reducing permeability. It would not be appropriate to conjecture hydrate pore habits based on permeability measurements. The results suggest pore connectivity controlled by overall hydrate distribution would be critical for permeability compared to the hydrate pore habit within pores.

4 Conclusions

Single phase flow is simulated through pore structures extracted from laboratory synthesized methane hydrate-bearing specimens. Results are compared with the widely used models based on idealized pore habits. Pore-scale analysis and observations reveal that the geometric assumptions

in the well-known grain-coating or pore-filling models should be modified to be more realistic. Future models should consider that hydrate particles are always in contact with sediment particles with contact angles dependent on excess-gas or excess-water environments, neither forming a uniform layer with the same thickness nor floating in the center of pores. Although simulation results are close to the prediction of pore-filling in specimens with relatively homogeneous distributed hydrate, we highlight this is caused by other mechanisms: (1) hydrate particles at low saturation protrude into the pore structure and efficiently reduce the flow velocity; (2) at high saturation, hydrate particles block most paths and the flow is restricted to less paths. The influence of formation method or intra-pore habit of hydrate on permeability of hydrate-bearing sediments is not obvious. By contrast, inter-pore hydrate distribution has a much higher impact on the permeability and uneven hydrate distribution can result in drastic permeability anisotropy.

Acknowledgments

Lingli Pan and Liang Lei are supported under an ORISE fellowship granted by National Energy Technology Laboratory. Figures and table host all of the data used within the manuscript and are available for download through Figshare (https://doi.org/10.6084/m9.figshare.12551669).

References

Ayachit, U. (2015). *The ParaView Guide: A Parallel Visualization Application*. NY, United States: Kitware, Inc.

Berg, S., Kutra, D., Kroeger, T., Straehle, C. N., Kausler, B. X., Haubold, C., et al. (2019). ilastik: interactive machine learning for (bio)image analysis. *Nature Methods, 16*(12), 1226-1232. https://doi.org/10.1038/s41592-019-0582-9

Berge, L. I., Jacobsen, K. A., & Solstad, A. (1999). Measured acoustic wave velocities of R11 (CCl3F) hydrate samples with and without sand as a function of hydrate concentration.

Journal of Geophysical Research: Solid Earth, *104*(B7), 15415-15424. https://doi.org/10.1029/1999JB900098

Boswell, R. (2009). Is gas hydrate energy within reach? *Science*, *325*(5943), 957-958. https://doi.org/10.1126/science.1175074

Boswell, R., & Collett, T. S. (2011). Current perspectives on gas hydrate resources. *Energy & Environmental Science*, *4*(4), 1206-1215. https://doi.org/10.1039/C0EE00203H

Chaouachi, M., Falenty, A., Sell, K., Enzmann, F., Kersten, M., Haberthür, D., & Kuhs, W. F. (2015). Microstructural evolution of gas hydrates in sedimentary matrices observed with synchrotron X-ray computed tomographic microscopy. *Geochemistry, Geophysics, Geosystems*, *16*(6), 1711-1722. https://doi.org/10.1002/2015GC005811

Chen, X., & Espinoza, D. N. (2018). Ostwald ripening changes the pore habit and spatial variability of clathrate hydrate. *Fuel*, *214*, 614-622. https://doi.org/10.1016/j.fuel.2017.11.065

Chen, X., Verma, R., Espinoza, D. N., & Prodanović, M. (2018). Pore-Scale Determination of Gas Relative Permeability in Hydrate-Bearing Sediments Using X-Ray Computed Micro-Tomography and Lattice Boltzmann Method. *Water Resources Research*, *54*(1), 600-608. https://doi.org/10.1002/2017WR021851

Dai, S., Santamarina, J. C., Waite, W. F., & Kneafsey, T. J. (2012). Hydrate morphology: Physical properties of sands with patchy hydrate saturation. *Journal of Geophysical Research: Solid Earth*, *117*(B11), B11205. https://doi.org/10.1029/2012JB009667

Dai, S., & Seol, Y. (2014). Water permeability in hydrate‐bearing sediments: A pore‐scale study. *Geophysical Research Letters*, *41*(12), 4176-4184. https://doi.org/10.1002/2014GL060535

Delli, M. L., & Grozic, J. L. H. (2014). Experimental determination of permeability of porous media in the presence of gas hydrates. *Journal of Petroleum Science and Engineering*, *120*, 1-9. https://doi.org/10.1016/j.petrol.2014.05.011

Fang, Y., Flemings, P. B., Daigle, H., Phillips, S. C., Meazell, P. K., & You, K. (2020). Petrophysical properties of the GC 955 hydrate reservoir inferred from reconstituted sediments: Implications for hydrate formation and production. *AAPG Bulletin*. https://doi.org/10.1306/01062019165

Gerke, K. M., Vasilyev, R. V., Khirevich, S., Collins, D., Karsanina, M. V., Sizonenko, T. O., et al. (2018). Finite-difference method Stokes solver (FDMSS) for 3D pore geometries: Software development, validation and case studies. *Computers & Geosciences*, *114*, 41-58. https://doi.org/10.1016/j.cageo.2018.01.005

Johnson, A., Patil, S., & Dandekar, A. (2011). Experimental investigation of gas-water relative permeability for gas-hydrate-bearing sediments from the Mount Elbert Gas Hydrate Stratigraphic Test Well, Alaska North Slope. *Marine and Petroleum Geology*, *28*(2), 419-426. https://doi.org/10.1016/j.marpetgeo.2009.10.013

Kikinis, R., Pieper, S. D., & Vosburgh, K. G. (2014). 3D Slicer: a platform for subject-specific image analysis, visualization, and clinical support. In Jolesz, F. A. (Ed.), *Intraoperative Imaging and Image-Guided Therapy* (pp. 277-289). New York, NY: Springer. https://doi.org/10.1007/978-1-4614-7657-3_19

Kleinberg, R. L., Flaum, C., & Collett, T. S. (2005). *Magnetic resonance log of JAPEX/JNOC/GSC et al. Mallik 5L-38 gas hydrate production research well: gas hydrate saturation, growth habit, and relative permeability*. Geological Survey of Canada, Northwest Territories, Canada. https://doi.org/10.4095/220860

303 Kleinberg, R. L., Flaum, C., Griffin, D. D., Brewer, P. G., Malby, G. E., Peltzer, E. T., &
304 Yesinowski, J. P. (2003). Deep sea NMR: Methane hydrate growth habit in porous media
305 and its relationship to hydraulic permeability, deposit accumulation, and submarine slope
306 stability. *Journal of Geophysical Research: Solid Earth, 108*(B10), 2508.
307 https://doi.org/10.1029/2003JB002389
308 Kneafsey, T. J., Seol, Y., Gupta, A., & Tomutsa, L. (2011). Permeability of laboratory-formed
309 methane-hydrate-bearing sand: Measurements and observations using X-ray computed
310 tomography. *SPE Journal, 16*(01), 78-94. https://doi.org/10.2118/139525-PA
311 Konno, Y., Yoneda, J., Egawa, K., Ito, T., Jin, Y., Kida, M., et al. (2015). Permeability of
312 sediment cores from methane hydrate deposit in the Eastern Nankai Trough. *Marine and*
313 *Petroleum Geology, 66*, 487-495.
314 Kumar, A., Maini, B., Bishnoi, P. R., Clarke, M., Zatsepina, O., & Srinivasan, S. (2010).
315 Experimental determination of permeability in the presence of hydrates and its effect on
316 the dissociation characteristics of gas hydrates in porous media. *Journal of Petroleum*
317 *Science and Engineering, 70*(1), 114-122. https://doi.org/10.1016/j.petrol.2009.10.005
318 Lee, M. W. (2008). *Models for gas hydrate-bearing sediments inferred from hydraulic*
319 *permeability and elastic velocities*. U.S. Geological Survey, Denver, CO.
320 https://pubs.usgs.gov/sir/2008/5219/pdf/SIR08-5219_508.pdf
321 Lei, L., Liu, Z., Seol, Y., Boswell, R., & Dai, S. (2019a). An investigation of hydrate formation
322 in unsaturated sediments using X-ray computed tomography. *Journal of Geophysical*
323 *Research: Solid Earth, 124*(4), 3335-3349. https://doi.org/10.1029/2018JB016125
324 Lei, L., & Seol, Y. (2019). High-saturation gas hydrate reservoirs – A pore scale investigation of
325 their formation from free gas and dissociation in sediments. *Journal of Geophysical*
326 *Research: Solid Earth, 124*(12), 12430-12444. https://doi.org/10.1029/2019JB018243
327 Lei, L., & Seol, Y. (2020). Pore-scale investigation of methane hydrate-bearing sediments under
328 triaxial condition. *Geophysical Research Letters, 47*(5), e2019GL086448.
329 https://doi.org/10.1029/2019GL086448
330 Lei, L., Seol, Y., Choi, J.-H., & Kneafsey, T. J. (2019b). Pore habit of methane hydrate and its
331 evolution in sediment matrix – Laboratory visualization with phase-contrast micro-CT.
332 *Marine and Petroleum Geology, 104*, 451-467.
333 https://doi.org/10.1016/j.marpetgeo.2019.04.004
334 Lei, L., Seol, Y., & Jarvis, K. (2018). Pore-scale visualization of methane hydrate-bearing
335 sediments with micro-CT. *Geophysical Research Letters, 45*(11), 5417-5426.
336 https://doi.org/10.1029/2018GL078507
337 Lei, L., Seol, Y., & Myshakin, E. M. (2019c). Methane hydrate film thickening in porous media.
338 *Geophysical Research Letters, 46*(20), 11091-11099.
339 https://doi.org/10.1029/2019GL084450
340 Li, X.-S., Xu, C.-G., Zhang, Y., Ruan, X.-K., Li, G., & Wang, Y. (2016). Investigation into gas
341 production from natural gas hydrate: A review. *Applied Energy, 172*, 286-322.
342 https://doi.org/10.1016/j.apenergy.2016.03.101
343 Liang, H., Song, Y., Chen, Y., & Liu, Y. (2011). The measurement of permeability of porous
344 media with methane hydrate. *Petroleum Science and Technology, 29*(1), 79-87.
345 https://doi.org/10.1080/10916460903096871
346 Liu, L., Liu, C., Li, C., Sun, J., Meng, Q., & Zhang, H. (2017). Determining the permeability of
347 hydrate-bearing slity-fine sands with water transient flow. In *International Geophysical*

Conference, Qingdao, China, 17-20 April 2017 (pp. 1335-1338): Society of Exploration Geophysicists and Chinese Petroleum Society. https://doi.org/10.1190/IGC2017-341

Mahabadi, N., Dai, S., Seol, Y., & Jang, J. (2019). Impact of hydrate saturation on water permeability in hydrate-bearing sediments. *Journal of Petroleum Science and Engineering, 174*, 696-703. https://doi.org/10.1016/j.petrol.2018.11.084

Makogon, Y. F. (1997). *Hydrates of hydrocarbons*. Tulsa, Oklahoma: Pennwell Books, PennWell Publishing Company.

Masuda, Y. (1997). Numerical calculation of gas-production performance from reservoirs containing natural gas hydrates. *Western Regional Meeting*, Long Beach, California.

Milkov, A. V. (2004). Global estimates of hydrate-bound gas in marine sediments: how much is really out there? *Earth-Science Reviews, 66*(3), 183-197. https://doi.org/10.1016/j.earscirev.2003.11.002

Minagawa, H., Egawa, K., Sakamoto, Y., Komai, T., Tenma, N., & Narita, H. (2012). Characterization of hydraulic permeability of methane-hydrate-bearing sediment estimated by T2-distribution of proton NMR. *The Twenty-second International Offshore and Polar Engineering Conference*, Rhodes, Greece.

Nanda, J., Shukla, K. M., Lall, M. V., Yadav, U. S., & Kumar, P. (2019). Lithofacies characterization of gas hydrate prospects discovered during the National Gas Hydrate Program expedition 02, offshore Krishna-Godavari Basin, India. *Marine and Petroleum Geology, 108*, 226-238. https://doi.org/10.1016/j.marpetgeo.2019.03.032

Phillips, S. C., Flemings, P. B., Holland, M. E., Schultheiss, P. J., Waite, W. F., Jang, J., et al. (2020). High concentration methane hydrate in a silt reservoir from the deep-water Gulf of Mexico. *AAPG Bulletin*. https://doi.org/10.1306/01062018280

Priest, J. A., Druce, M., Roberts, J., Schultheiss, P., Nakatsuka, Y., & Suzuki, K. (2015). PCATS Triaxial: A new geotechnical apparatus for characterizing pressure cores from the Nankai Trough, Japan. *Marine and Petroleum Geology, 66*, 460-470. https://doi.org/10.1016/j.marpetgeo.2014.12.005

Ren, X., Guo, Z., Ning, F., & Ma, S. (2020). Permeability of hydrate-bearing sediments. *Earth-Science Reviews, 202*, 103100. https://doi.org/10.1016/j.earscirev.2020.103100

Sakamoto, Y., Komai, T., Kawabe, Y., & Yamaguchi, T. (2003). Properties of multiphase flow in marine sediments with gas hydrate. *Fifth ISOPE Ocean Mining Symposium*, Tsukuba, Japan.

Santamarina, J. C., Dai, S., Terzariol, M., Jang, J., Waite, W. F., Winters, W. J., et al. (2015). Hydro-bio-geomechanical properties of hydrate-bearing sediments from Nankai Trough. *Marine and Petroleum Geology, 66*, 434-450. https://doi.org/10.1016/j.marpetgeo.2015.02.033

Singh, H., Myshakin, E. M., & Seol, Y. (2019). A nonempirical relative permeability model for hydrate-bearing sediments. *SPE Journal, 24*(02), 547-562. https://doi.org/10.2118/193996-PA

Sloan, E. D., & Koh, C. A. (2007). *Clathrate hydrates of natural gases (Third edition)* (Heinemann, H. Ed.). Boca Raton, FL: CRC Press. https://www.crcpress.com/Clathrate-Hydrates-of-Natural-Gases-Third-Edition/Sloan-Jr-Koh/p/book/9780849390784

Wang, Y., Feng, J.-C., Li, X.-S., Zhang, Y., & Chen, Z.-Y. (2018). Fluid flow mechanisms and heat transfer characteristics of gas recovery from gas-saturated and water-saturated hydrate reservoirs. *International Journal of Heat and Mass Transfer, 118*, 1115-1127. https://doi.org/10.1016/j.ijheatmasstransfer.2017.11.081

You, K., Flemings, P. B., Malinverno, A., Collett, T. S., & Darnell, K. (2019). Mechanisms of methane hydrate formation in geological systems. *Reviews of Geophysics, 57*(4), 1146-1196. https://doi.org/10.1029/2018RG000638

Test No.	S_h [%]	n [%]	P [MPa]	T [°C]	$k_{0,x}$ [μm²]	$k_{0,y}$ [μm²]	$k_{0,z}$ [μm²]	$k_{e,x}$ [μm²]	$k_{e,y}$ [μm²]	$k_{e,z}$ [μm²]	k_x [%]	k_y [%]	k_z [%]	Sand Type	Formation
1	8.0	30.8	13.8	4.5	12.63	11.95	12.28	5.37	4.85	5.25	42.5	40.6	42.8	Ottawa	Excess-gas
2	11.6	38.0	13.8	12	33.94	31.10	39.34	23.38	9.92	26.03	68.9	31.9	66.2	Ottawa	
3	25.2	35.8	12.4	10	26.06	23.26	25.65	8.74	7.14	8.76	33.5	30.7	34.2	Ottawa	
4	39.5	37.4	10.7	5	27.28	28.04	32.14	1.67	2.31	2.60	6.1	8.2	8.1	Ottawa	
5	48.2	38.8	12.4	10	16.08	12.99	15.48	2.23	1.16	2.78	13.9	8.9	17.9	Mixture	
6	51.6	44.5	12.4	10	9.03	8.66	9.14	0.37	0.21	0.23	4.1	2.4	2.5	F110	
7	57.2	36.6	13.8	6.5	46.64	47.05	43.99	1.40	2.29	1.89	3.0	4.9	4.3	Ottawa	
8	68.1	35.0	13.8	7.4	41.02	34.87	37.81	0.77	0	0	1.9	0	0	Ottawa	
9	75.0	36.0	13.8	6.5	37.55	37.07	36.68	0	0	0	0	0	0	Ottawa	
10	86.5	32.5	13.8	6.5	26.14	25.37	27.57	0	0	0	0	0	0	Ottawa	
11	41.1	35.8	12.4	10	26.06	23.26	25.65	2.21	1.21	2.15	8.5	5.2	8.4	Ottawa	Excess-water from excess-gas
12	51.5	38.8	12.4	10	16.08	12.99	15.48	1.11	0.51	1.47	6.9	3.9	9.5	Mixture	
13	55.2	36.6	14.1	6.5	46.88	47.20	44.22	1.14	1.03	1.14	2.4	2.2	2.6	Ottawa	
14	56.8	37.4	10.7	5	27.28	28.04	32.14	0.51	0.74	1.12	1.9	2.6	3.5	Ottawa	
15	75.8	44.5	12.4	10	9.03	8.66	9.14	0	0	0	0	0	0	F110	
16	24.7	36.7	17.2	12	40.91	37.65	39.43	15.60	14.24	13.86	38.1	37.8	35.2	Ottawa	Excess-water
17	41.9	32.7	24.1	8.5	11.81	10.97	11.85	0.21	3.38	3.18	1.8	30.8	26.8	Ottawa	
18	43.5	37.4	10.3	4	27.28	28.04	32.14	2.32	2.01	2.20	8.5	7.2	6.8	Ottawa	
19	71.5	33.4	24.1	8.5	13.79	12.98	13.43	0	0	0.14	0	0	1.0	Ottawa	
20	71.9	36.7	24.1	8.5	42.50	40.32	42.08	0.23	0.04	0.08	0.5	0.1	0.2	Ottawa	
21	89.6	33.7	24.1	8.5	13.40	11.73	12.62	0	0	0	0	0	0	Ottawa	

S_h = Hydrate Saturation; n = Porosity; P = Pore Pressure; T = Temperature; k_0 = intrinsic permeability; k_e = effective permeability; k = normalized permeability; Ottawa = Ottawa Sand with ~250 μm mean diameter; F110 = F110 Sand with ~120 μm mean diameter; Mixture = Specimen with a layer of Ottawa sand and a layer of F110 sand.

Excess-gas: Sand is mixed with water and packed into a column-shaped specimen. Methane pressure and temperature are adjusted to the targeted values to form methane hydrate with constant pressure gas supply. Excess-water from excess-gas: Brine is flushed through hydrate-bearing specimens formed under excess-gas condition. Excess-water: High pressure methane is introduced to water-saturated specimens, then temperature is reduced and hydrate forms with constant pressure water supply.

Table 1

Information of hydrate-bearing specimens used in this study.

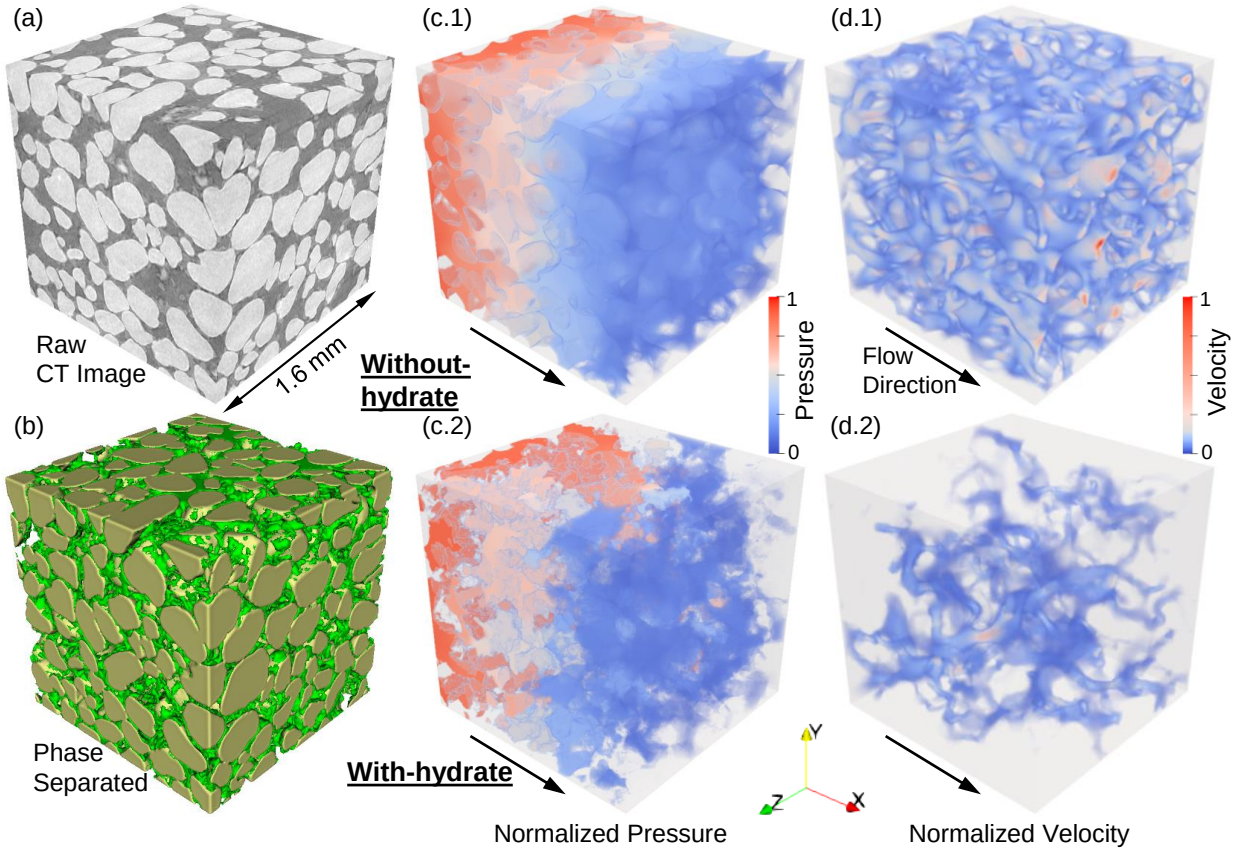

Figure 1

Procedure from raw CT image to pressure and velocity fields of fluid flow through specimens (Test 4, excess-gas condition, S_h = 39.5%). (a) Raw 3D micro-CT image. (b) 3D pore structures after segmentation: sand particles in brown, hydrate in green, and free methane transparent. (c) Normalized pressure fields with a flow direction along the X axis. (d) Normalized velocity fields with a flow direction along the X axis. (c.1-d.1) is Without-hydrate case and (c.2-d.2) is With-hydrate case.

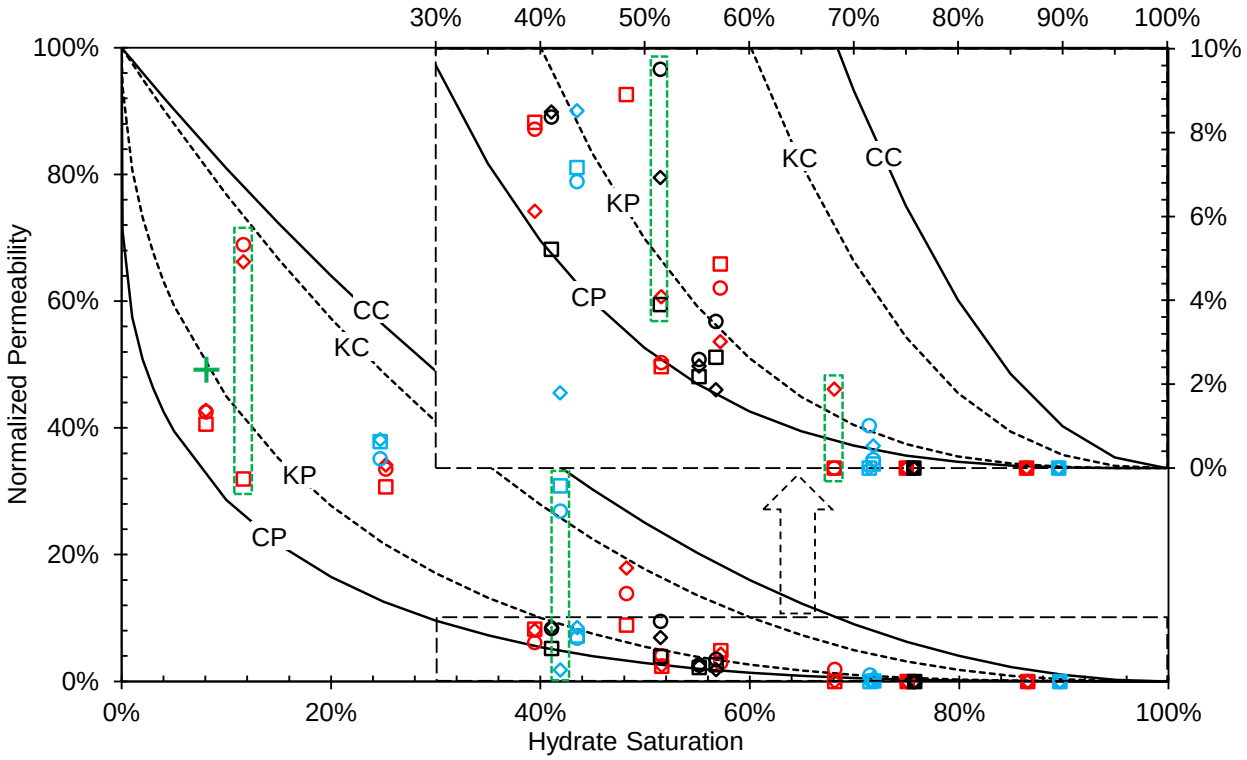

Figure 2

Normalized permeability from numerical simulations as a function of hydrate saturation. CC = Capillary-tube Coating, KC = Kozeny-grain Coating, KP = Kozeny-grain Pore-filling, and CP = Capillary-tube Pore-filling (Kleinberg et al., 2013). Symbols are results on conditions of excess-gas (red), excess-water from excess-gas by fluid injection (blue) and excess-water (black) as summarized in Table 1, and ◇, □ and ○ represent permeability in X, Y, and Z direction. The green + shows the result in Figure 3b. Vertical green frames highlight permeability anisotropy.

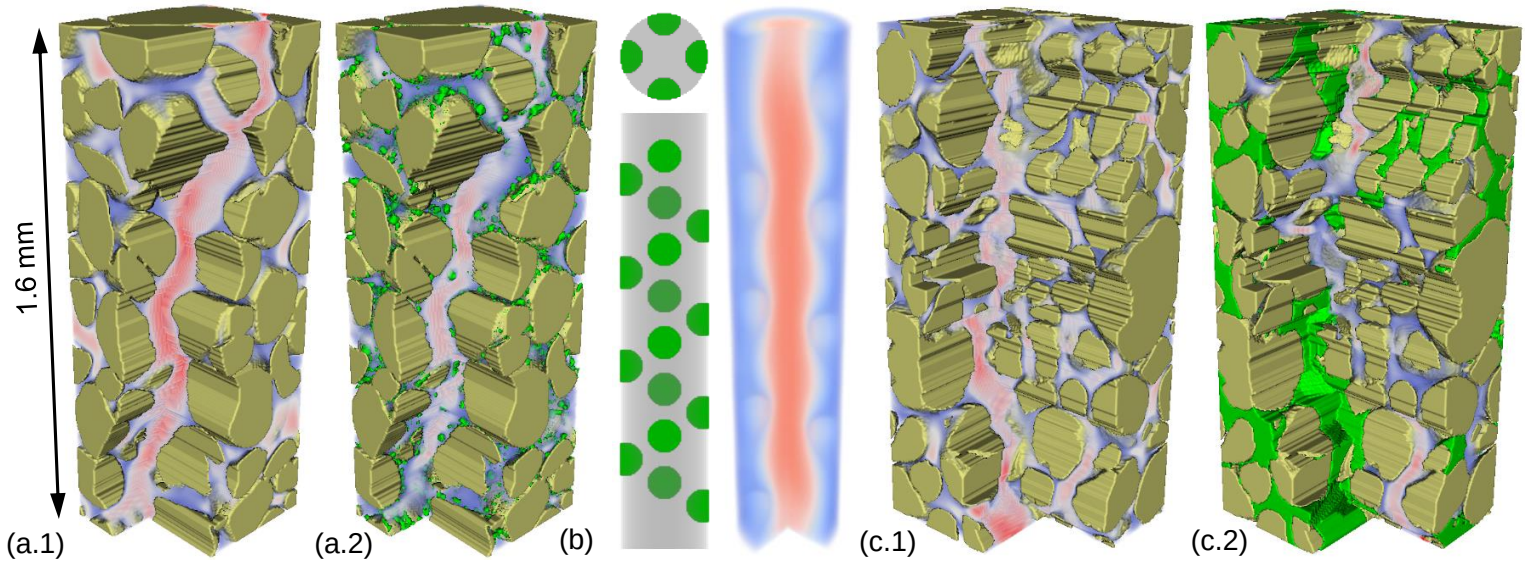

424

425 **Figure 3**

426 Effect of hydrate on geometry of flow path and velocity fields. (a) and (c) show the effect of actual hydrate distribution with hydrate

427 saturation of 8.0% (Test 1) and 71.5% (Test 19). (b) presents the effect of hydrate with idealized distribution mimicking that in (a).

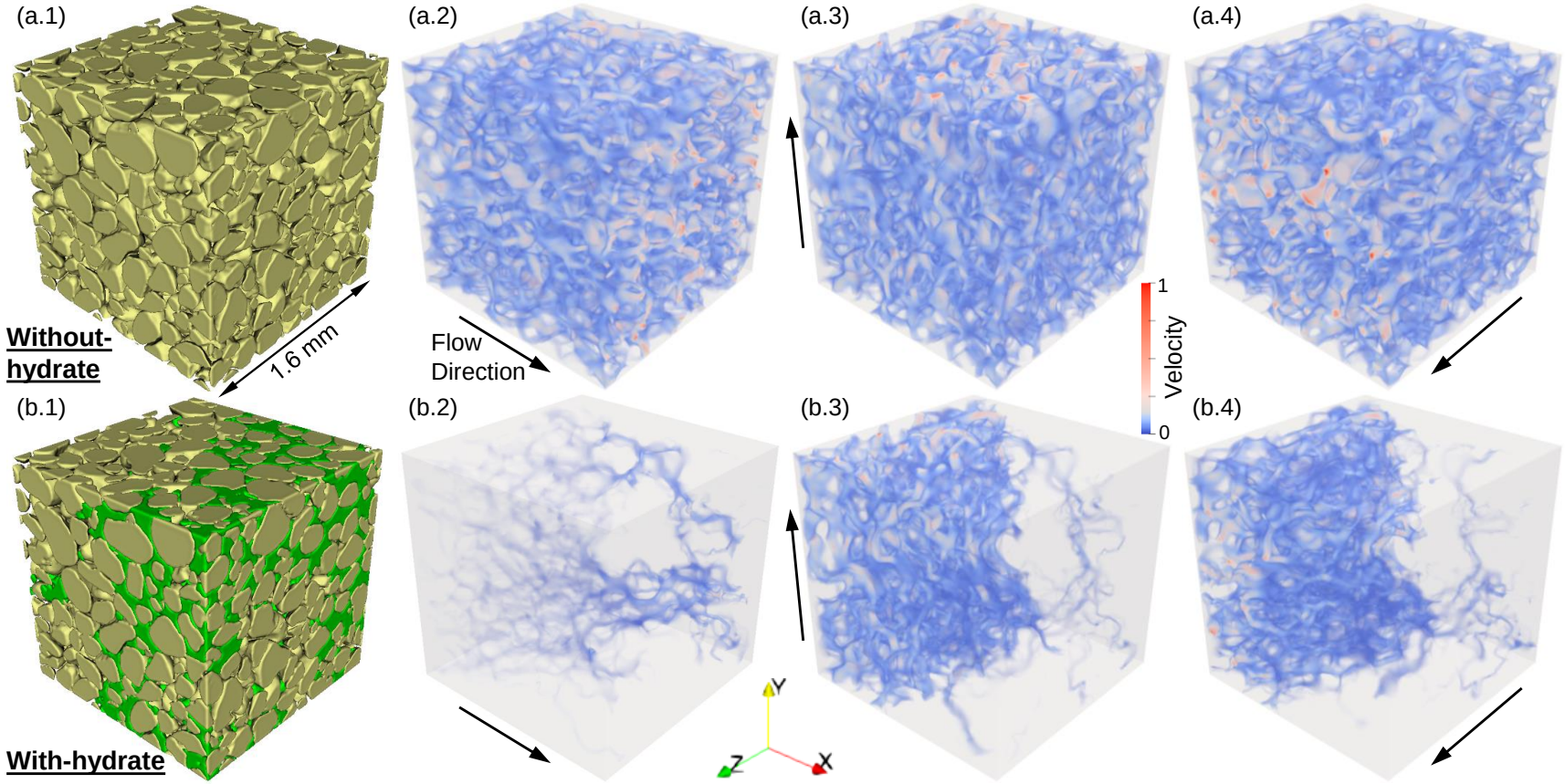

Figure 4

Unevenly distributed hydrate induced permeability anisotropy (Test 17, S_h = 41.9%). (a-b) show Without-hydrate case and With-hydrate case. (a/b.1-a/b.4) present 3D pore structure, and flow velocity fields along X, Y and Z directions.

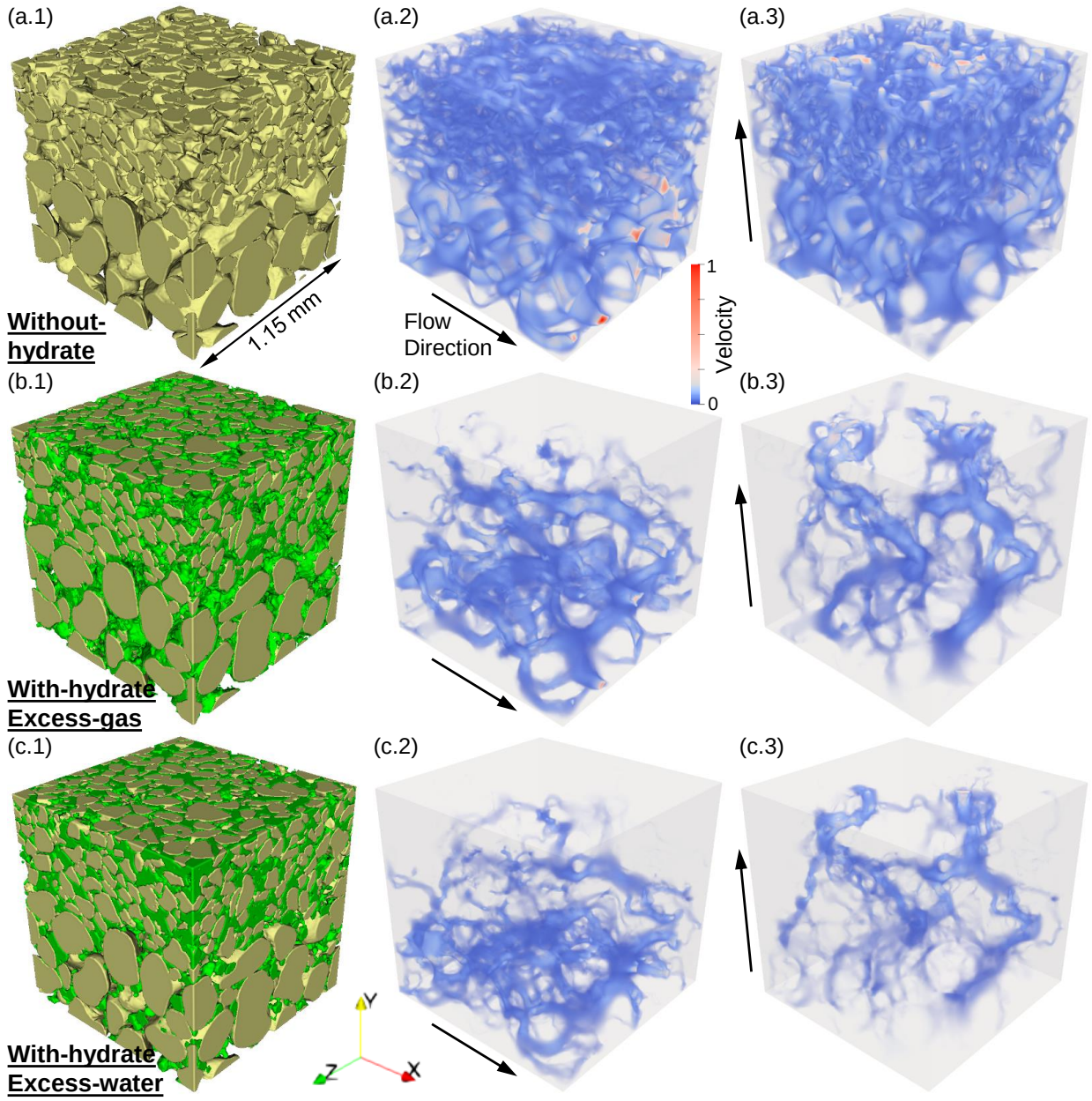

Figure 5

Permeability in layered systems. (a-c) show cases of Without-hydrate, With-hydrate under excess-gas condition (Tests 5, S_h = 48.2%) and excess-water condition (Tests 12, S_h = 51.5%). (a/b/c.1-a/b/c.3) present 3D pore structures, and flow velocity fields along X and Y directions.